Enhanced Hysteresis-Based Current Regulators in Vector Control of DFIG Wind Turbines

Mansour Mohseni, *Student Member, IEEE*, Syed M. Islam, *Senior Member, IEEE*, and Mohammad A. S. Masoum, *Senior Member, IEEE*

Abstract—This paper proposes enhanced hysteresis-based current regulators in the field-oriented vector control of doubly fed induction generator (DFIG) wind turbines. The proposed control scheme is synchronized with the virtual grid-flux space vector, readily extractable by a quadrature phase-locked loop (QPLL) system. Identical equidistant-band vector-based hysteresis current regulators (VBHCRs) are then used to control the output currents of the rotor-side and grid-side converters. The proposed hysteresis-based technique has excellent steady-state performance and reveals several advantages in comparison with the commonly used proportional-integral (PI) current regulator, including very fast transient response, simple control structure, and intrinsic robustness to the machine parameters variations. Moreover, the fixed hysteresis bands in VBHCRs are replaced with equidistant bands to limit the instantaneous variations of the switching frequency and reduce the maximum switching frequencies experienced in the converters. Extensive simulation studies are carried out for a 1.5 MW DFIG-based wind turbine to examine the operation of the proposed vector control scheme under changing wind speed and compare its transient and steady-state performances with the conventional PI current regulators.

Index Terms—Doubly fed induction generator (DFIG), equidistant hysteresis bands, grid-flux orientation, vector-based hysteresis current regulator.

NOMENCLATURE

Vectors and Symbols

$\mathbf{V}, \mathbf{I}, \boldsymbol{\Phi}$	Voltage, current, and flux vectors.
ω, θ	Angular speed and angle.
L_m, L_σ	Mutual and leakage inductances.

Subscripts

$d-q$	Synchronous grid-flux frame.
s, r, g	Stator, rotor, and grid.
$x-y$	Rotor frame.
$\alpha-\beta$	Stationary frame.

Superscripts

a, s, r, e	Arbitrary, stationary, rotor, and grid-flux reference frames.
$*$	Reference value for the controllers.

I. INTRODUCTION

THE past decade has seen the emergence of wind as the world's most dynamically growing energy source. Wind energy conversion systems (WECS) are mainly divided into fixed- and variable-speed technologies. Variable-speed WECS have recently become more popular due to several advantages compared to the fixed-speed concepts, including maximized power capture, reduced mechanical stresses imposed on the turbine, improved power quality, and reduced acoustical noise [1]. The variable-speed technologies can be further subdivided into two major concepts: synchronous generators with full-scale converters and doubly fed induction generators (DFIGs). For high-power applications, the DFIG concept is more economically viable as it implements back-to-back voltage source converters (VSCs) rated at 30%–35% of the generator size for a given rotor speed variation range of ±25%.

Field-oriented vector control, using rotational transformations, and linear proportional-integral (PI) controllers, has so far proved to be the most popular technique used in DFIG-based wind turbines [2]–[4]. In this double-closed-loop approach, the outer power control loop is employed to attain an independent control over the active and reactive powers of the machine. Synchronous-frame PI current controllers are then used in cascade with the outer control loop to regulate the rotor output current. The phase angle of the stator-flux space vector is usually used in the literature for the controller synchronization, estimated through an open-loop observer [4]–[7]. However, if the stator-flux-oriented frame (SFOF) is adopted, the overall performance of the vector control scheme will be highly dependent on the accurate detection of the stator-flux position. This can be a critical problem under the distorted supply voltage condition or varying machine parameters. The virtual grid-flux-orientated frame (GFOF) has been introduced to address this problem [6]. In this method, the stator resistance is neglected as compared to the stator reactance, and the grid voltage vector is assumed to be vertically positioned with respect to the stator-flux space vector. Therefore, simple phase-locked loop (PLL) systems can be used to readily extract the synchronization signal from the grid voltage signal. It is also proven that by using the GFOF, the system stability and damping are independent of the rotor current [7].

On the other hand, there are two drawbacks associated with implementing PI current regulators in DFIG-based wind turbines: the discrete operation of the converters is not taken into account and the DFIG is modeled as a linear time-invariant (LTI) system. Based on these simplifying assumptions, the gains of PI controllers are tuned using the small signal analysis of the

nonlinear equations describing the DFIG behavior [8], [9]. Consequently, the system formulation is only valid around a specific operating condition and the response will deviate if the operation point varies. This will lead to the nonoptimal behavior of the overall control scheme over a wide operation range. The problem becomes especially crucial for wind generator applications, where the machine are required to properly function at the operating points largely deviated from the nominal condition, e.g., voltage sag/swell conditions requested in modern grid codes [10]. Therefore, the gains of the PI controller must be carefully designed with a tradeoff between maintaining the system stability over the whole operation range and achieving adequate dynamic response under transient conditions. This will noticeably degrade the transient performance of the overall vector control scheme and jeopardize the stability of the controller under changing operation conditions.

Nonlinear control approaches, such as direct torque/power control (DTC/DPC) methods, have been proposed to address the aforementioned problems [11]–[13]. In these techniques, the current control loop is eliminated and the control signal (the output voltage) is directly selected from a look-up table, aimed to control both active and reactive powers during a sample time. The main advantages of DTC/DPC methods are the enhanced transient response, minimum use of the machine parameters, and noncomplex control structure. However, there is always a significant torque/power ripple due to the high bandwidth of the controller, the converter switching frequency varies depending on the operation conditions, and the controller performance may deteriorate during the machine starting and low-speed operations. Modified methods have been proposed to overcome these problems [14]–[18], but extra drawbacks were introduced, such as the inclusion of additional PI controllers [15], [16], reduced robustness to the machine parameters variations [14]–[16], and complex online calculation requirements [17], [18].

Based on the same principle used in DTC/DPC, Xu *et al.* have suggested replacing the conventional PI current regulator with a nonlinear predictive current regulator [19]. The proposed current regulator calculates the variation of the rotor current vector at the end of each fixed sampling period and based on the estimated error, the output voltage vector of the rotor-side converter (RSC) is selected to eliminate the current errors at the end of the following sample period. Finally, the gating signals of the RSC are generated by a space vector modulation (SVM) unit. This method is fully compatible with digital control platforms and shows a very fast transient response and an excellent robustness under various operation conditions. However, its performance depends on the accurate estimation of the machine parameters and it suffers from a complex control structure.

This paper overcomes the aforementioned deficiencies by implementing equidistant-band vector-based hysteresis current regulators (VBHCRs) in the vector control of DFIG wind turbines. This current regulator was originally proposed by the authors for the conventional VSCs, showing a superior performance under the steady-state and transient operation conditions [20]. It was demonstrated that the proposed VBHCR retains the inherent advantages of the conventional hysteresis method (such as the excellent transient performance, simple
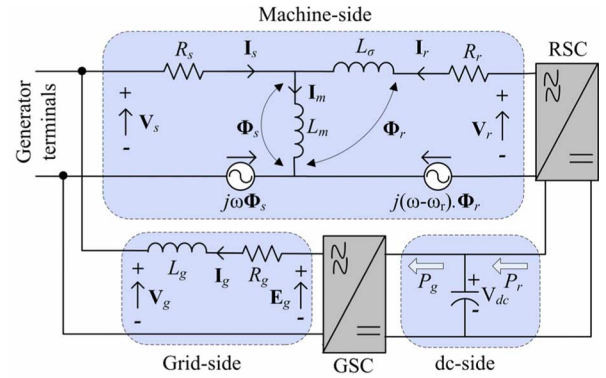

Fig. 1.   Equivalent circuit of the DFIG system.

hardware implementation, outstanding stability, and robustness to the machine parameters variations), but removes its severe disadvantages in three-phase applications (such as very high average switching frequency (ASF) and large oscillations in the output current) [20]. Moreover, the proposed VBHCR is superior to other vector-based methods proposed in the literature, since it avoids the redundant control actions observed in [21] and [22], has a simpler structure as compared to [23], and suppresses the current vector oscillations more effectively than the methods reported in [24] and [25]. The fixed hysteresis bands in the proposed VBHCR are replaced with equidistant bands to limit the instantaneous variations of the switching frequency and reduce the maximum switching frequencies (MSFs) experienced in the converters.

II. DFIG SYSTEM MODELING

The DFIG-based WECS are constituted of a wound-rotor induction machine (WRIM) mechanically coupled to the wind turbine. The stator winding is directly connected to the coupling transformer, whereas the rotor winding is connected through back-to-back partial-scale VSCs. A common dc-link capacitor is placed between the RSC and the grid-side converter (GSC). In this technology, the machine operation is fully controlled through the RSC, while the GSC is mainly targeted to keep the dc-link voltage constant. This section presents the machine and GSC modeling, followed by the discrete formulation of the output voltage vectors of converters.

A. Machine Modeling

Induction machines are usually modeled using the well-known "T-form" equivalent circuit with self- and mutual inductances [2]–[4]. However, the T-form equivalent circuit is more complex than necessary. Therefore, this paper uses a more convenient "Γ-form" equivalent circuit without losing the model accuracy [26]. The Γ-form equivalent circuit is graphically presented in Fig. 1 (the machine-side), where ω is the angular speed of the arbitrary reference frame. According to this model, the stator and rotor voltage vectors are defined by

$$\mathbf{V}_s^a = R_s \mathbf{I}_s^a + \frac{d\mathbf{\Phi}_s^a}{dt} + j\omega \cdot \mathbf{\Phi}_s^a \qquad (1)$$

$$\mathbf{V}_r^a = R_r \mathbf{I}_r^a + \frac{d\mathbf{\Phi}_r^a}{dt} + j(\omega - \omega_r) \cdot \mathbf{\Phi}_r^a \qquad (2)$$

and the flux vector are defined by

$$\mathbf{\Phi}_s^a = L_m (\mathbf{I}_s^a + \mathbf{I}_r^a) = L_m \mathbf{I}_m^a \qquad (3)$$

$$\mathbf{\Phi}_r^a = L_\sigma \mathbf{I}_r^a + L_m (\mathbf{I}_s^a + \mathbf{I}_r^a). \qquad (4)$$

Using (3) and (4), the rotor flux vector can be eliminated in (2), giving

$$\mathbf{V}_r^a = R_r \mathbf{I}_r^a + L_\sigma \frac{d\mathbf{I}_r^a}{dt} + \frac{d\mathbf{\Phi}_s^a}{dt} + j(\omega - \omega_r) \cdot (L_\sigma \mathbf{I}_r^a + \mathbf{\Phi}_s^a). \qquad (5)$$

Also, the output power of the stator winding can be expressed as follows:

$$\mathbf{S}_s^a = P_s + jQ_s = -1.5 \mathbf{V}_s^a \cdot \hat{\mathbf{I}}_s^a \qquad (6)$$

where $\hat{}$ is the complex conjugate operator.

B. GSC Modeling

The GSC mainly aims to keep the dc-link voltage constant while if desired, it can also provide a limited reactive power support. According to dc-side model shown in Fig. 1, the differential equation describing the capacitor voltage is given as follows:

$$CV_{dc} \frac{dV_{dc}}{dt} = P_r - P_g. \qquad (7)$$

In (7), the rotor power P_r is an independent variable that is controlled by the outer power control loop of the RSC. Therefore, the dc-link voltage can be controlled only through the GSC active power P_g. If the power losses in the ac filter of the GSC are neglected, the output power of the GSC can be defined as follows:

$$\mathbf{S}_g^a = P_g + jQ_g = 1.5 \mathbf{V}_g^a \cdot \hat{\mathbf{I}}_g^a. \qquad (8)$$

Also, referring to the GSC-side model in Fig. 1, the voltage equation of this converter in the arbitrary frame can be expressed by

$$\mathbf{E}_g^a = R_g \mathbf{I}_g^a + L_g \frac{d\mathbf{I}_g^a}{dt} + \mathbf{V}_g^a. \qquad (9)$$

From (9), it can be observed that the operation of the GSC is identical to the conventional grid-connected VSCs [20].

C. Discrete Formulation of the Output Voltage Vectors of Converters

The power circuit of the RSC is shown in Fig. 2(a). At each instant, the output voltage vector of the converter is defined based on the three-phase gating signals, i.e., S_a^*, S_b^*, and S_c^*. In phase a, the current is flowing through the upper switch (S_1) if $S_a^* = 1$. Otherwise, the lower switch (S_4) is conducting, the phase current ($S_a^* = 0$). Using the same definitions for phases b and c, the output voltage vector generated by the RSC can be defined by

$$\mathbf{V}_r = \frac{1}{3} V_{dc} [(2S_a^* - 1) + \exp(j2\pi/3) \cdot (2S_b^* - 1)$$
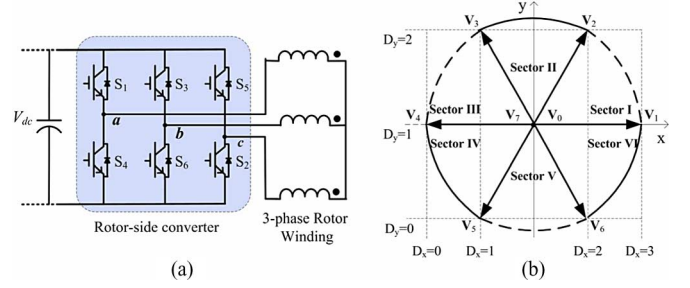$$+ \exp(-j2\pi/3) \cdot (2S_c^* - 1)]. \qquad (10)$$

Fig. 2. (a) Power circuit of the RSC. (b) Discrete representation of the RSC output voltage vector.

TABLE I
THREE-PHASE SWITCHING STATES, RSC OUTPUT VOLTAGE VECTOR, AND RESPECTIVE x–y COMPONENTS

S_a^*	S_b^*	S_c^*	$\mathbf{V}_r$	V_x/V_{dc}	V_y/V_{dc}
0	0	0	$\mathbf{V}_0$	0	0
1	0	0	$\mathbf{V}_1$	2/3	0
1	1	0	$\mathbf{V}_2$	1/3	$1/\sqrt{3}$
0	1	0	$\mathbf{V}_3$	-1/3	$1/\sqrt{3}$
0	1	1	$\mathbf{V}_4$	-2/3	0
0	0	1	$\mathbf{V}_5$	-1/3	$-1/\sqrt{3}$
1	0	1	$\mathbf{V}_6$	1/3	$-1/\sqrt{3}$
1	1	1	$\mathbf{V}_7$	0	0

If all the possible combinations of gating signals are considered in (10), eight switching states, and consequently, eight output voltage vectors are obtained, given by

$$\begin{cases} \mathbf{V}_r = \frac{2}{3} V_{dc} \exp(j(k-1) \cdot \pi/3), k = 1, 2, \ldots, 6 \\ \mathbf{V}_r = \mathbf{V}_0 = \mathbf{V}_7 = 0. \end{cases} \qquad (11)$$

Based on (11), the available discrete output voltage vectors consist of six nonzero ($\mathbf{V}_1 - \mathbf{V}_6$) and two zero ($\mathbf{V}_0$ and $\mathbf{V}_7$) voltage vectors, defined in Table I and displayed in Fig. 2(b) [20]. Similar discrete definitions can be developed for the GSC.

III. PROPOSED VECTOR CONTROL SCHEME OF DFIG

A. Grid-Flux Orientation

The SFOF is the most popular synchronization technique used in the vector control of DFIG-based wind turbines. In this method, the d-axis of the synchronous frame is fixed to the stator-flux space vector and rotates anticlockwise at the speed of ω_s, as displayed in Fig. 3(a). However, this synchronization technique needs the accurate estimation of the stator-flux space vector at each instant. As an alternative, if (1) is rewritten in the stationary frame, it can be observed that the space vectors of $\mathbf{V}_g$ and $\mathbf{\Phi}_s$ are positioned almost orthogonally, with a small drift due to the voltage drop across the stator resistance. In medium and large induction machines, the stator resistance is very small compared to the stator reactance ($R_s \leq 0.01 L_s$). Therefore, the q-axis of the stator-flux frame is practically aligned with the grid-voltage space vector, and in turn, the instantaneous position of the grid voltage vector can be used for the synchronization without any significant error [27]. Instead of directly using the grid voltage vector, this paper utilizes the virtual grid-flux space vector ($\mathbf{\Phi}_g$) to fully acknowledge the principle of the vector control
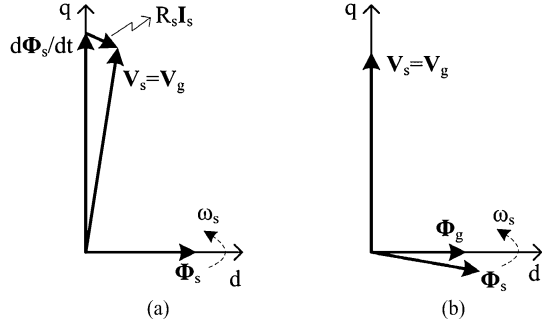
Fig. 3. Phasor diagrams for field-oriented vector control of DFIG. (a) Conventional SFOF. (b) Proposed GFOF.

method that requires a flux-linkage space vector for the synchronization [5], [6]. In this method, the d-axis of the proposed synchronous frame will be aligned with the nonmeasurable grid flux space vector, as shown in Fig. 3(b). Note that unlike the conventional stator-flux-orientation approach, the phase angle of the proposed synchronous frame can be readily extracted using a well-known PLL system, since the grid-voltage and the grid-flux space vectors are positioned vertically. Therefore, the space vector relationships between the stationary frame, the rotor frame rotating at ω_r, and the grid-voltage frame rotating at ω_s can be defined by

$$\mathbf{F}^e = \mathbf{F}^s \cdot e^{-j\omega_s t} = \mathbf{F}^s \cdot e^{-j\theta_s} \tag{12}$$

$$\mathbf{F}^r = \mathbf{F}^e \cdot e^{j(\omega_s - \omega_r)t} = \mathbf{F}^e \cdot e^{j\theta_{\text{slip}}} \tag{13}$$

where $\mathbf{F}$ represents a voltage, current, or flux space vector.

Conventional PLL techniques cannot present accurate phase-angle estimation under asymmetrical fault conditions because the second harmonics produced by the negative-sequence component of the grid voltage will propagate through the PLL system and will be reflected in the extracted phase angle [28]. To avoid this problem, a quadratic PLL (QPLL) system, with an outstanding immunity to noise, harmonic, and unbalance distortions, has been used in this paper [29]. The proposed QPLL system produces a clean synchronization signal extracted from the positive-sequence component of the grid voltage. Structural simplicity and performance robustness are other salient features of the proposed QPLL.

B. Vector Control of the RSC

The stator voltage vector in the virtual GFOF can be expressed by $\mathbf{V}_s^e = jV_{sq}$, as shown in Fig. 3(b). Therefore, based on (6), the active and reactive powers of the stator winding can be defined as follows [4]:

$$P_s = -1.5V_{sq}I_{sq} = 1.5V_{sq}I_{rq} \tag{14a}$$

$$Q_s = -1.5V_{sq}I_{sd} = 1.5V_{sq}\left(I_{rd} - \frac{V_{sq}}{\omega_s L_m}\right). \tag{14b}$$

From (14), it can be observed that the independent control of the stator active and reactive powers can be achieved through regulating the q and d components of the rotor current vector, respectively. Therefore, the RSC controller can be configured, as shown in Fig. 4.

1) Clarke's transformation is used to obtain the vector representation of the measured three-phase signals, i.e., to convert from ($I_{s-3\varnothing}$ and $V_{s-3\varnothing}$) to ($\mathbf{V}_s^s$ and $\mathbf{I}_s^s$) and from $I_{r-3\varnothing}$ to $\mathbf{I}_r^r$.
2) The rotor angle is directly measured using a high-resolution position encoder, whereas the synchronizing signal (the grid-voltage phase angle) is extracted using the QPLL system.
3) The stator voltage and stator current vectors are transformed from the stationary frame to the GFOF, using (12).
4) Using (14a) and (14b), the active and reactive powers produced in the stator winding are calculated and compared to their command values. The command signal of the active power (P^*) is calculated based on the optimal power–speed curve given by the wind turbine manufacturer and the angular speed of the rotor at each instant (ω_r) [30]. On the other hand, the Q^* signal is usually defined based on the grid-code requirements imposed by the system operator [10].
5) The error signals ΔP_s and ΔQ_s are fed to the PI control blocks in order to calculate the I_{rq}^* and I_{rd}^* signals, respectively. The rotor command vector ($\mathbf{I}_r^{e*}$) is then transformed from the GFOF to the rotor reference frame, using (13).
6) Finally, the rotor command vector ($\mathbf{I}_r^{r*}$) along with the measured current vector ($\mathbf{I}_r^r$) are fed to the proposed hysteresis-based current regulator to directly generate the appropriate gating signals for the RSC.

C. Vector Control of the GSC

The GSC is controlled using a similar grid-flux-oriented vector control scheme. If (8) is rewritten in the GFOF, the active and reactive powers of the GSC can be obtained as follows:

$$P_g = 1.5V_{gq}I_{gq} \tag{15}$$

$$Q_g = 1.5V_{gq}I_{gd}. \tag{16}$$

Substituting (15) in (7) defines the variations of the dc-link voltage as follows:

$$CV_{\text{dc}}\frac{dV_{\text{dc}}}{dt} = P_r - 1.5V_{gq}I_{gq}. \tag{17}$$

In (17), the grid voltage is constant under normal operation conditions and the rotor power is to be controlled by the RSC. Thus, the variation of the dc-link voltage can be only controlled through the q component of the GSC current (I_{gq}). On the other hand, the reactive power of the GSC is controlled through the d component of the current vector. Therefore, the GSC vector controller can be configured, as shown in Fig. 4.

1) Two PI control blocks are used to calculate the I_{gq}^* and I_{gd}^* current components from the error signals of ΔV_{dc} and ΔQ_g, respectively.
2) The GSC current command vector ($\mathbf{I}_g^{e*}$) is transferred from the GFOF to the stationary frame, using (12).
3) Finally, Clarke's transformation is used to obtain the vector representation of the measured GSC three-phase current ($I_{g-3\phi}^s$). The consequent current vector ($\mathbf{I}_g^s$) along with the current command vector ($\mathbf{I}_g^{s*}$) are fed to the
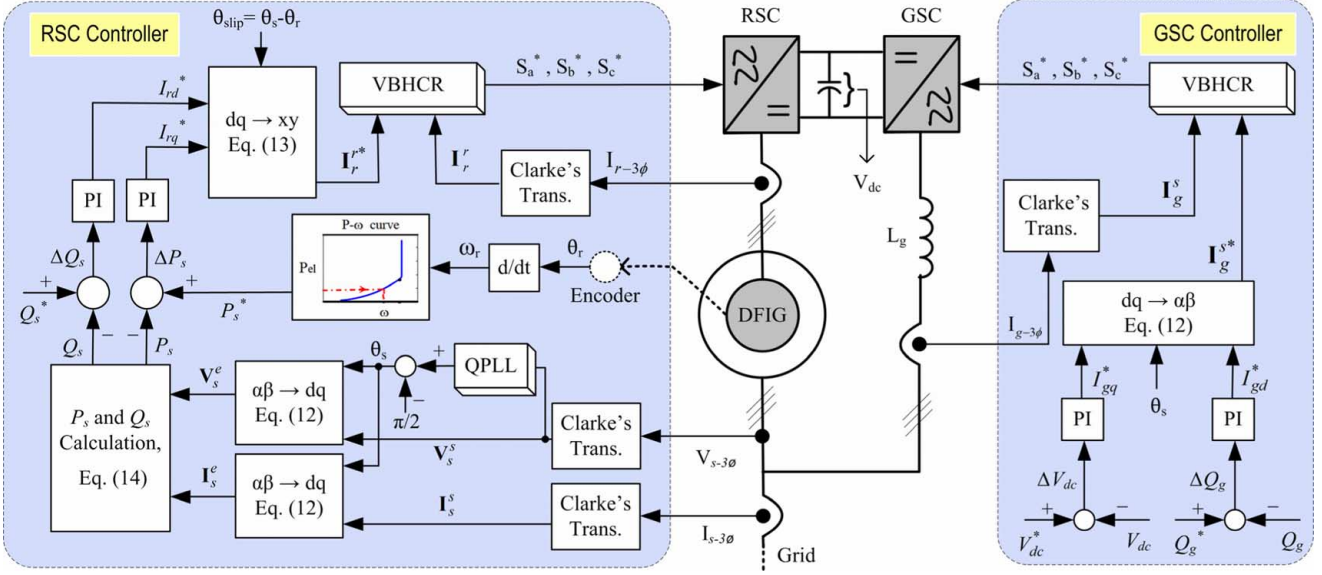
Fig. 4. Schematic diagram of the proposed grid-flux-oriented vector control scheme for DFIG-based WECS.

proposed equidistant-band VBHCR to generate appropriate gating signals in the GSC.

IV. IMPLEMENTATION OF THE PROPOSED VBHCR IN DFIG

Two identical equidistant-band VBHCRs have been used to control the output current of the RSC and GSC. It was discussed that the utilization of the proposed current regulator in the GSC is similar to the conventional grid-connected VSCs. This issue has been comprehensively studied in [20] and is not repeated here. Instead, this paper explores the principle and the practical implementation of the proposed VBHCR in the RSC of DFIG-based WECS.

A. Principle of the Proposed VBHCR Implemented in the RSC

The proposed VBHCR is designed to control the output current of the RSC in the rotor reference frame. Therefore, the RSC output voltage must be expressed in the x–y frame. Substituting $\omega = \omega_r$ in (5) results in

$$\mathbf{V}_r^r = R_r \mathbf{I}_r^r + L_\sigma \frac{d\mathbf{I}_r^r}{dt} + \frac{d\mathbf{\Phi}_s^r}{dt}. \tag{18}$$

If the current error vector is defined as $\mathbf{I}_{r,e}^r = \mathbf{I}_r^{r*} - \mathbf{I}_r^r$, the differential equation describing this vector can be derived as follows:

$$L_\sigma \frac{d\mathbf{I}_{r,e}^r}{dt} + R_r \mathbf{I}_{r,e}^r = L_\sigma \frac{d\mathbf{I}_r^{r*}}{dt} + R_r \mathbf{I}_r^{r*} - (\mathbf{V}_r^r - \mathbf{e}_0^r) \tag{19}$$

where $\mathbf{e}_0^r = d\mathbf{\Phi}_s^r/dt$ is the back electromotive force (EMF) voltage vector. Based on (19), the current error vector changes with the time constant of L_σ/R_r and is influenced by the current command vector and its derivative, as well as, the RSC output voltage and the back EMF voltage vectors. If the rotor resistance is neglected in (19), the desired output voltage vector to nullify the current error vector can be expressed by

$$\mathbf{V}_r^{r*} = \mathbf{e}_0^r + L_\sigma \frac{d\mathbf{I}_r^{r*}}{dt}. \tag{20}$$
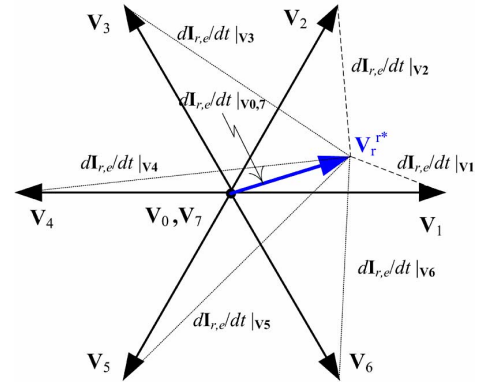
Fig. 5. Derivatives of the current error when the $\mathbf{V}_r^{r*}$ vector is located in Sector I.

Substituting (20) in (19) gives

$$L_\sigma \frac{d\mathbf{I}_{r,e}^r}{dt} = \mathbf{V}_r^{r*} - \mathbf{V}_r^r. \tag{21}$$

From (20) and (21), it is clear that the information about back EMF voltage vector and derivative of current command vector are required to nullify the tracking error in the RSC. However, it is not practically easy to measure the back EMF voltage vector or current derivatives. An indirect technique has been used in this paper to tackle the problem and extract the required information from the desired output voltage vector [24]. Suppose that the $\mathbf{V}_r^{r*}$ space vector is located in Sector I in Fig. 2(b). Based on (21), the error derivative vectors with respect to various output voltage vectors of the RSC ($\mathbf{V}_0 - \mathbf{V}_7$) can be defined, as shown in Fig. 5. Small current deviations ($d\mathbf{I}_{r,e}^r/dt$) are required to follow the current command with the minimum possible switching frequency. That is, the voltage space vectors adjacent to $\mathbf{V}_r^{r*}$ must be applied in the RSC to attain the desired optimal switching pattern, e.g., $\mathbf{V}_1$, $\mathbf{V}_2$, $\mathbf{V}_0$, and $\mathbf{V}_7$ in Sector I. If this switching pattern is to be generated in
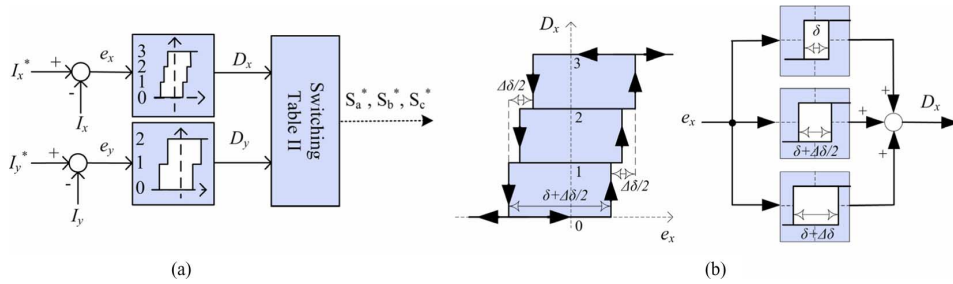
Fig. 6.   (a) Implementation of the proposed VBHCR in the RSC. (b) Four-level hysteresis comparator.

the RSC, the two adjacent nonzero voltage vectors along with $\mathbf{V}_0$ and $\mathbf{V}_7$ are the only vectors that will be selected to reduce the tracking error. Therefore, the resulting switching pattern will be similar to the well-known SVM technique under the steady-state condition [24]. On the other hand, for fast tracking response under transient conditions, nonzero voltage vectors with high-current error derivatives must be applied to force the RSC output current inside the hysteresis bands as fast as possible. Note that the proposed switching method operates based on the sector position of the $\mathbf{V}_r^{r*}$ vector, not the exact value of the vector.

B. Practical Implementation of the Proposed VBHCR

Referring to Table I, it is observed that the output voltage vector of the RSC can have four and three different values in the x- and y-axes, respectively. This fact can be used to equally divide the rotor complex frame into six $60°$ sectors, as shown in Fig. 2(b). Accordingly, the proposed VBHCR employs four-level and three-level hysteresis comparators for the x- and y-current tracking errors, as displayed in Fig. 6(a). Digital outputs of comparators (D_x and D_y) are then fed to the switching table in order to calculate the RSC output voltage vector at each instant. Fig. 6(b) shows the practical implementation of the four-level hysteresis comparator, with the overall bandwidth of $\delta + \Delta\delta$ used in the x-axis.

The bandwidths of hysteresis comparators are tuned based on the tracking accuracy requested from the current regulator. Smaller hysteresis bands give more restricted oscillations in the RSC output current, but it is achieved at the expense of higher switching frequencies. Therefore, there is always a trade-off between the controller tracking accuracy and the consequent switching frequency.

It can be observed that the proposed current regulator is a robust method because it only uses local measurements of the current and is independent of system parameters. Also, it has inherent current limiting properties and very fast transient response, since it directly controls the instantaneous value of the rotor current. The implementation of this method is very simple and the computation time minimal [20].

For every one-sixth of the fundamental period, both x and y comparators remain in one specific hysteresis loop, which can be used to detect the sector position of the $\mathbf{V}_r^{r*}$ vector. Then, zero voltage vectors and two nonzero voltage vectors adjacent to $\mathbf{V}_r^{r*}$ will be selected to reduce the tracking error of the RSC. For example, suppose that x and y comparators are located in the middle and the top hysteresis loops, respectively,

TABLE II
SWITCHING TABLE FOR THE PROPOSED VBHCR

D_x \ D_y	0	1	2
0	$\mathbf{V}_5$	$\mathbf{V}_4$	$\mathbf{V}_3$
1	$\mathbf{V}_5$	$\mathbf{V}_0$	$\mathbf{V}_3$
2	$\mathbf{V}_6$	$\mathbf{V}_0$	$\mathbf{V}_2$
3	$\mathbf{V}_6$	$\mathbf{V}_1$	$\mathbf{V}_2$

i.e., $D_x = 1$ or 2 and $D_y = 1$ or 2. According to Table II, the $\mathbf{V}_r^{r*}$ position is detected in Sector II and the optimal voltage sequence of $\mathbf{V}_0, \mathbf{V}_2, \mathbf{V}_3$, and $\mathbf{V}_7$ will be selected to be applied in the RSC. Under these circumstances, if $e_x = I_x^* - I_x$ and $e_y = I_y^* - I_y$ hit the higher hysteresis bands of $\delta + \Delta\delta/2$ and $\delta + \Delta\delta$, respectively, digital outputs of comparators will become equal to $D_x = 2$ and $D_y = 2$. This requires the $\mathbf{V}_2$ voltage vector to be generated by the RSC in order to increase both x and y components of the rotor current. Likewise, if $D_x = 1$ and $D_y = 2$, the $\mathbf{V}_3$ vector must be applied to reduce the I_{rx} component and simultaneously increase the I_{ry} component. Zero voltage vectors must be selected in other cases. Further reduction in the switching frequency can be attained by the appropriate selection of the zero voltage vector between $\mathbf{V}_0$ and $\mathbf{V}_7$. The $\mathbf{V}_0$ vector must be chosen if the present output voltage vector of the RSC is equal to $\mathbf{V}_1, \mathbf{V}_3$, or $\mathbf{V}_5$. In this case, only one inverter leg must be switched to obtain the zero voltage vector in the RSC output. In the same way, the $\mathbf{V}_7$ vector will be selected if the RSC state comes from $\mathbf{V}_2, \mathbf{V}_4$, or $\mathbf{V}_6$.

As the time passes, either the x or y comparator will move to the next hysteresis loop. This indicates that the position of the $\mathbf{V}_r^{r*}$ vector has changed to the next sector in the rotor frame; therefore, a new optimal switching sequence must be selected from Table II. The resulting switching pattern will be constituted of six four-state optimal voltage vectors sets, which matches with six $60°$ sectors of the fundamental period. It is, therefore, clear that the proposed VBHCR generates an optimal switching pattern similar to the widely used SVM technique that significantly reduces the ASF of the RSC and suppresses the oscillations in the output current vector.

C. Equidistant Hysteresis Bands

The proposed VBHCR considerably reduces the ASF by the systematic application of zero voltage vectors. However, the instantaneous switching frequency varies widely during the fundamental period and may exceed the safety limits of the converter

switches (insulated gate bipolar transistors) at certain conditions, specifically near the zero crossing points of the reference current. Therefore, lock-out circuits must be incorporated to limit the MSF, leading to severe current distortions and large error overreaches. This problem partly arises from uneven lateral distance of hysteresis bands during the fundamental period. Very high switching frequencies occur around zero crossing points because the lateral distance of hysteresis bands is much smaller near those points as compared to the peaks of the reference current. Two types of variable hysteresis bands have been proposed in the literature to address this problem and reduce the MSF of converter: adaptive and equidistant hysteresis bands. The former removes interphases dependency and achieve fixed switching frequency with low-current ripples [31]–[33]. However, adaptive hysteresis bands typically require extra signal processing and complex control structure, suffer from stability problems, and show degraded transient performance [33]. The equidistant hysteresis bands, on the other hand, are very simple methods to reduce the MSF and limit the instantaneous variations of the switching frequency of converter [34]. Fixed switching frequency is not achieved, but the simplicity, outstanding stability, and very fast transient response of the conventional hysteresis method are retained. It is evident that the vector-based method and equidistant hysteresis bands are complementary when applied to the converters of DFIG.

In this paper, the fixed hysteresis bands in the proposed VBHCR are replaced with the equidistant bands introduced in [34]. In this method, a suitable percentage of the band height is subtracted at areas close to the peaks, giving almost even lateral distance from upper and lower bands during the fundamental period. The equidistant hysteresis band (λ') is defined by

$$\lambda' = \frac{\lambda}{1-k} \left[1 - |k \sin(\theta_r)| \right] \qquad (22)$$

where k is a constant with the optimal value of 0.3 [34]. If the equidistant bands defined in (22) are used in the proposed VBHCR, a more homogenous switching pattern will be generated with smaller variations of the instantaneous switching frequency over the fundamental period and smaller MSFs near the zero crossing points of the reference current.

V. SIMULATION RESULTS

Simulation studies have been carried out in the three main directions listed in [35]: 1) the operation of the proposed vector control scheme under changing wind speed is thoroughly examined; 2) the steady-state performance of the proposed VBHCR is compared with the widely used PI current regulator; and 3) the transient responses of current regulators are compared under asymmetrical grid fault condition.

Fig. 7 shows the schematic diagram of the simulated system with the parameters given in the Appendix. Equidistant hysteresis bands have been used in the simulation studies and the bandwidths of comparators are set to $\delta = \Delta\delta + \Delta\delta = 0.02$ p.u. in the RSC and $\delta = \Delta\delta = 0.0125$ p.u. in the GSC, respectively. Using these parameters, an acceptable tradeoff between the current tracking accuracy and the consequent switching frequency has been obtained in the RSC and GSC.
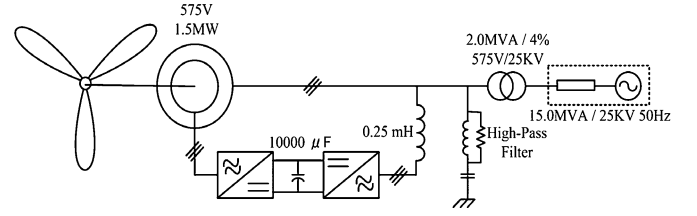

Fig. 7. Circuit diagram of the simulated network.

A. Operation Under Changing Wind Speed

In the first step, the mechanical input torque to the DFIG is externally specified in order to emulate the power extracted by the wind turbine. Also, the lumped inertia constant of the system is intentionally set to the very small value of 0.025 s to have similar mechanical and electrical time constants and obtain a better illustration. Figs. 8 and 9 show the simulation results with a ramped-up wind speed between 0.3 and 0.5 s and a step change in the reactive power command to –0.2 MVAR at $t = 0.7$ s.

For $0.1 < t < 0.3$ s, the wind speed is equal to 7.8 m/s, the machine rotates at $\omega_r = 0.9$ p.u. based on the simulated optimal power–speed curve, and the active power of 0.4 MW is generated in the stator winding. However, since the DFIG rotates at subsynchronous speed with $s = +0.1$, 10% of the active power generated in the stator winding is fed back to the machine through the converters [30]. Accordingly, the proposed grid-flux-oriented vector control scheme regulates (I_{rd} and I_{rq}) to (0.35, 0.3) p.u. and (I_{gd} and I_{gq}) to (0, –0.02) p.u., in order to attain the desired active and reactive powers production in the stator winding and the GSC. The three-phase rotor current ($I_{r-3\varphi}$) rotates with the slip frequency of 5 Hz ($\omega_{\text{slip}} = \omega_s - \omega_r = 0.1$ p.u.), whereas the GSC current ($I_{g-3\varphi}$) always has the fundamental frequency of 50 Hz, imposed by the grid. Therefore, the position of $\mathbf{V}_r^{r*}$ and $\mathbf{V}_g^{s*}$ voltage vectors change in an incremental order from Sector I to Sector VI with $f_r = 0.1$ p.u. = 5 Hz and $f_g = 1.0$ p.u. = 50 Hz, respectively.

As the wind speed ramps up to 10.5 m/s between $t = 0.3$ and 0.5 s, the rotor accelerates from 0.9 to 1.2 p.u. and the active power production of the DFIG system increases to 0.9 MW. The machine operates in the supersynchronous mode; thus, the active power is delivered to the grid through both stator and rotor windings ($P_s = 0.75$ MW and $P_g = 0.15$ MW). Note that changes in the active power of the stator winding and the GSC have been obtained through the variations in q components of the command current signals, while the d components are kept constant. Similarly, the I_{rd}^* component has been decreased from 0.35 to 0.1 p.u. at $t = 0.7$ s to change the reactive power of the stator winding from 0 to –0.2 MVAR. This demonstrates the independent control of the active and reactive powers by the proposed grid-flux-oriented vector control scheme.

For $t > 0.5$ s, the three-phase rotor current rotates with the frequency of 10 Hz ($\omega_{\text{slip}} = \omega_s - \omega_r = -0.2$ p.u.), where the negative sign of the slip frequency is manifested in the reversal of the sequence of the three-phase current flowing in the rotor winding (from *a–b–c* to *a–c–b*). As a result, the $\mathbf{V}_r^{r*}$ position rotates clockwise from Sector VI to Sector I with $f = 10$ Hz,
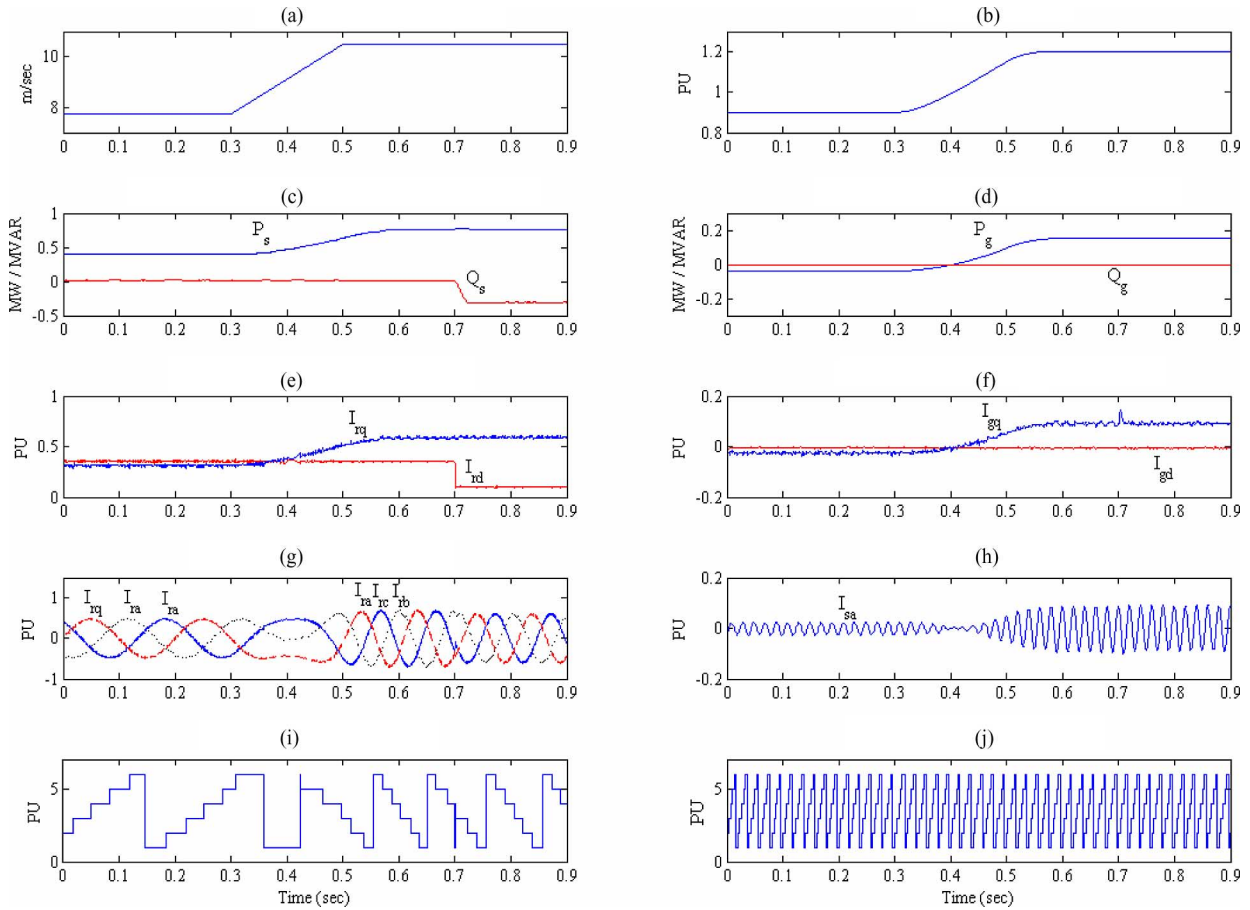
Fig. 8.   Simulation results when the wind speed varies from 7.8 to 10.5 m/s. (a) Wind speed. (b) Rotor speed. (c) Active/reactive powers in the stator winding. (d) Active/reactive powers in the GSC. (e) RSC current vector in the GFOF. (f) GSC current vector in the GFOF. (g) 3-Phase rotor current ($I^r_{r-3\Phi}$). (h) Stator phase curent ($I^s_{s-\Phi}$). (i) Region of the V^{r*}_r vector. (j) Region of the V^{s*}_g vector.

while the $\mathbf{V}^{s*}_g$ position still changes incrementally from Sector I to Sector VI with $f = 50$ Hz. It is finally worth noting that during the synchronous operation around $t = 0.4$ s, no active power is transferred from back-to-back converters connected to the rotor. Therefore, the GSC current amplitude decreases to almost zero and the $\mathbf{V}^{r*}_r$ position is held unchanged in Sector I.

Simulation results, presented in Fig. 8, show the excellent tracking performance of the proposed current regulator under extremely demanding conditions, i.e., under very fast variations of the wind speed over short period of time (0.2 s). Similar observations can be made for the DFIG operation under random wind speed variations in longer periods of time.

Fig. 9 shows the detailed operation of the proposed equidistant-band VBHCR subjected to a step change in I^*_{rd} at $t = 0.7$ s. Both x and y comparators are first located in the lowest hysteresis loop, i.e., $D_x = 0$ or 1 and $D_y = 0$ or 1. According to Table II, this indicates that the $\mathbf{V}^{r*}_r$ vector is positioned in Sector IV and the optimal switching sequence of $\mathbf{V}_0$, $\mathbf{V}_4$, $\mathbf{V}_5$, and $\mathbf{V}_7$ is selected to be applied in the RSC. In this case, Fig. 9(a) and (b) shows that the proposed VBHCR effectively keeps the tracking error (e_x and e_y) within the inner hysteresis bands of δ. The digital outputs of multilevel comparators and the consequent switching pattern of the RSC are shown in Fig. 9(c) and (d), respectively. It is clear that under the steady-state condition,

the zero voltage vectors are systematically applied in the RSC for most of the time, leading to a drastic reduction in the switching frequency of the RSC. Then, the I^*_{rd} changes at $t = 0.7$ s and the $\mathbf{V}^{r*}_r$ location jumps to Sector I due to the second term in (21). Under this transient condition, the proposed current hysteresis-based regulator selects the nonzero voltage vectors (e.g., the $\mathbf{V}_2$ vector) to quickly force the RSC output current vector back inside the hysteresis bands within a very short response time of 2 ms. Thereafter, the steady-state operation of the current regulator is followed in Sector III.

B. Comparison of the Steady-State Performances

The steady-state performances of the proposed VBHCR and the commonly used PI current regulator have been compared in terms of the harmonic distortions of the DFIG output current and the ASFs of converters. Optimal tuning of the PI controller gains is essential to attain an accurate comparison between the current regulators. Therefore, internal-mode control (IMC) is first used to have an educated guess about the PI gains, where the optimum bandwidth of the current control loop is estimated equal to 0.8 p.u., i.e., 10%–90% rise time of 10 ms [36]. Then, numerous trail-and-error simulation sets were conducted to obtain the most optimized gains in the PI units.
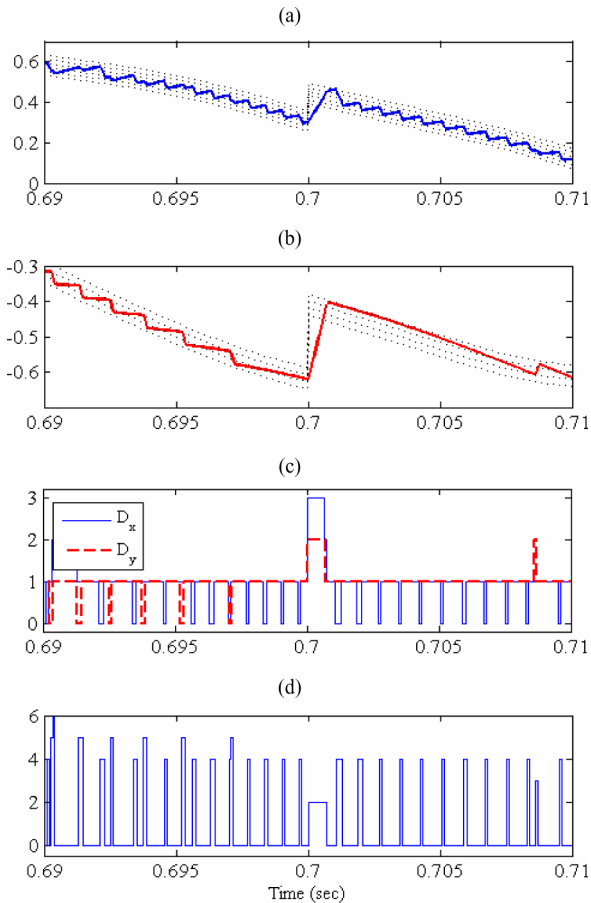
Fig. 9. Detailed operation of the proposed VBHCR subjected to a step change in I_{rd}^* (zero voltage vectors are shown as $\mathbf{V}_0$ for the sake of calrity). (a) I_{rx} and its corresponding hysteresis bands. (b) I_{ry} and its corresponding hysteresis bands. (c) Digital outputs of multi-level hysteresis comparators. (d) Output voltage vector of the RSC (V_r^r).

The harmonic content of the DFIG output current varies with the rotation speed of the machine and the most severe harmonic distortion is expected at the highest slip values when a larger proportion of the total machine current is transferred through the back-to-back converters. Therefore, the rotor speed has been set to 1.25 p.u. to examine the output current of the DFIG under the most severe operation condition. Fig. 10 shows the harmonic spectra when different current regulators have been used in the RSC and GSC (dashed lines show the IEEE Standard limits). In case of the PI current regulator, the total harmonic distortion (THD) is equal to 3.2% with a well-predictable frequency spectrum, where harmonic components only exist at frequency orders of $nf_{sw} \pm 1$ (e.g., 23rd, 25th, 47th, 49th, etc.) [20]. In contrast, the proposed equidistant-band VBHCR gives an output current with harmonic components spread over a wide frequency range and the THD of 4.1%. However, the THD level and the amplitudes of the individual harmonic components are still below the permitted distortion limits suggested in IEEE Standard 15471 and IEC Standards [37], [38].

Fig. 11 shows the number of switching in phase "a" of the RSC using different current regulators. The simulation time frames are set equal to twice the fundamental period of the rotor current, i.e., equal to 0.8 and 0.16 s when the DFIG operates with $s = 0.05$ and 0.25, respectively. It can be seen that for the VBHCR, the switching frequency stops rising for half of the fundamental period, as can be seen in the switching Table II [20]. ASFs of the RSC and GSC with various current regulators are summarized in Table III. It is evident that: 1) the PI current regulator gives a fixed switching frequency specified by the carrier waveform, e.g., 1200 Hz in this study; 2) the switching frequency of hysteresis-based methods varies with the rotation speed of the machine; 3) the highest switching frequencies will be observed when the converters are controlled by the conventional hysteresis method and the DFIG operates with high-slip values; (4) the switching frequency of the GSC is always larger than the RSC because more limited hysteresis bands have been used in the GSC; 5) the ASFs decrease by 30%–60% if the proposed vector-based current regulator is implemented in the RSC and GSC; and 6) a further reduction of 10%–30% can be attained when the fixed hysteresis bands are replaced with the equidistant bands. The main conclusion is that the proposed equidistant-band VBHCR will generally lead to smaller ASFs as compared to the conventional PI current regulator because wind generators are designed to rotate close to their synchronous speed for the most prevalent wind speed of the site. Further simulation studies have shown that by using equidistant hysteresis bands, the proposed current regulator can satisfactorily operate with the MSF limited to 6 kHz. This figure will increase to 10 kHz when the conventional fixed bands have been used in the proposed VBHCR.

C. Comparison of the Transient Performances

The transient responses of current regulators have been evaluated by simulating a single-phase to ground fault in the grid for $0.1 < t < 0.3$ s. Passing through the YΔ transformer, this fault causes a 60% type C voltage dip at the machine terminals, as shown in Fig. 12(a) [39]. Note that the outer power control loop has been deactivated and the rotor speed is fixed at 1.2 p.u. to perform an accurate comparison between the inner current control loops. Fig. 12(b) shows the rotor phase current when the conventional PI current regulator is used in the RSC. It can be seen that large transient overshoots with $f = f_r = 60$ Hz will appear in the rotor current at the fault onset, originated from the natural flux response [40]. In addition, the negative-sequence component of the grid voltage produces a 50% double-frequency ripple with $f = f_s + f_r = 2.2$ p.u. = 120 Hz in the rotor winding. The conventional PI current regulator cannot suppress these oscillations because this type of current regulator, with very limited control bandwidth, is not designed to provide the tracking speed required for high-frequency negative- and zero-sequence components. In contrast, the very fast transient response of the proposed VBHCR can handle the fault condition and effectively eliminate the transient overshoots or double-frequency ripples that tend to appear in the rotor winding during the dip. Fig. 12(c) shows that the operation of the proposed VBHCR is essentially independent of the grid voltage waveform.

On the other hand, it is well known that the negative-sequence currents are needed in the RSC and GSC to suppress
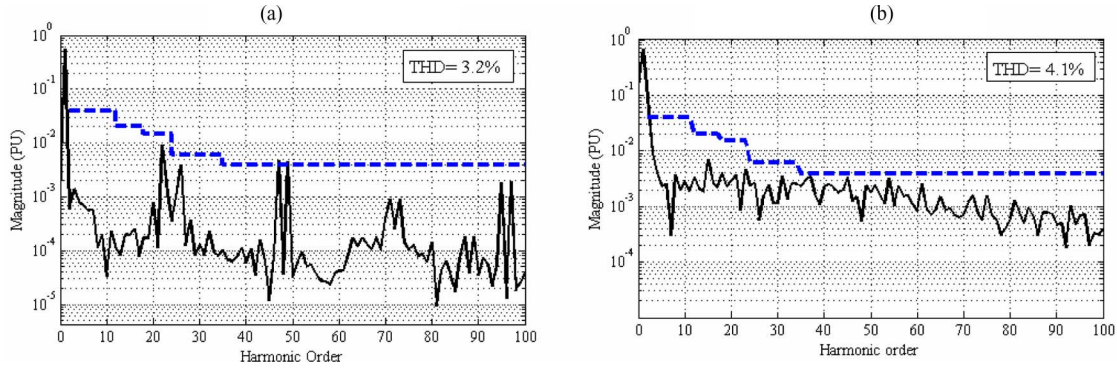
Fig. 10. Harmonic spectrum of the DFIG ouput current with (a) PI current regulator with $f_{sw} = 1200$ Hz. (b) Proposed equidistant-band VBHCR (dashed line: harmonic limits specified in [37]).
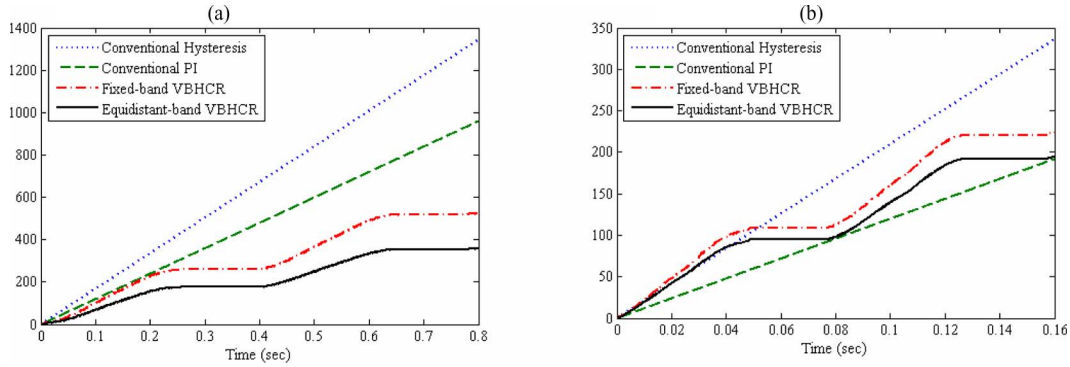

Fig. 11. Number of switching in phase "a" of the RSC when DFIG operates with (a) $s = 0.05$ and (b) $s = 0.25$.
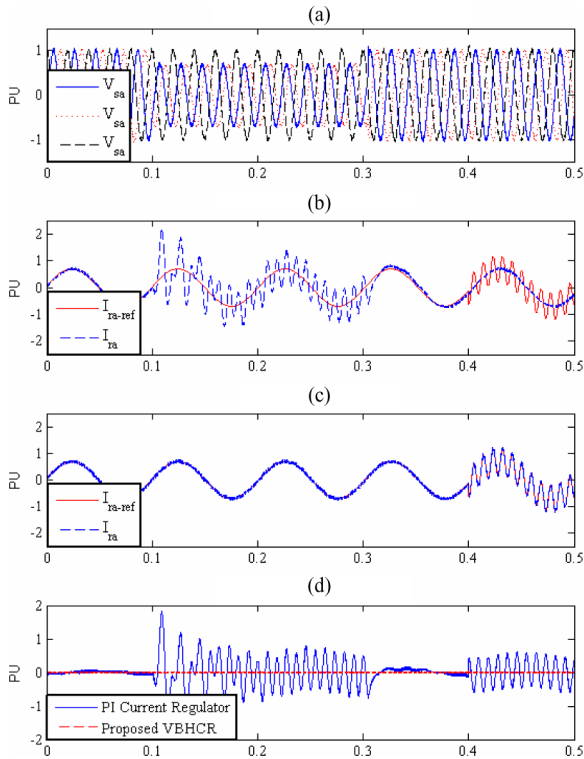

Fig. 12. Operation of various current regulators subjected to the single-phase to ground fault. (a) 3-Phase supply voltage. (b) PI current regulator. (c) Proposed VBHCR. (d) Current regulator error.

TABLE III
ASF IN THE RSC AND GSC USING VARIOUS CURRENT REGULATORS

Current Regulator	Conv. PI with SVM	Conv. HCR		Fixed-Band VBHCR		Equidistant-Band VBHCR	
	S= 0.0 or 0.025	S= 0.05	S= 0.25	S= 0.05	S= 0.25	S= 0.05	S= 0.25
RSC	1200	1680	2100	660	1410	450	1230
GSC	1200	1810	2400	780	1680	560	1430

the torque/active power oscillations and enhance the fault ride-through capability of the DFIG under various fault conditions [41]. Current regulators with complex control structure, e.g., additional negative-sequence control loop or resonant compensators, have been proposed in the literature for this purpose [41], [42]. A negative-sequence component is thus added to the reference current signal for $t > 0.4$ s to further examine the transient performance of the proposed VBHCR. In this case, the command signal is constituted of two components: the positive sequence with $f_+ = f_s - f_r = 0.2$ p.u. $= 10$ Hz and the high-frequency negative sequence with $f_- = f_s + f_r = 2.2$ p.u. $= 110$ Hz. It can be seen that the conventional PI current regulator can only follow the positive-sequence component of the command signal, whereas the proposed VBHCR can accurately follow both the positive- and the negative-sequence components. The tracking errors for both current regulators are shown in Fig. 12(d).

Finally, Fig. 13 compares the operation of the conventional and QPLL systems under the asymmetrical voltage dip
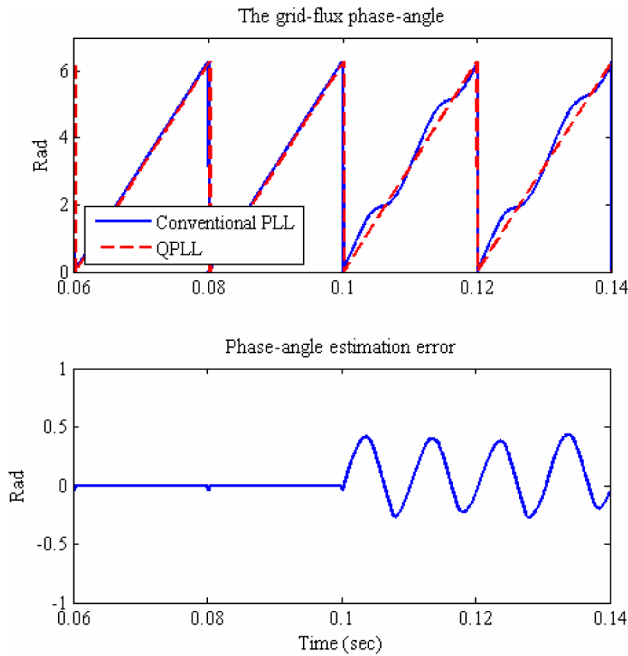
Fig. 13. Synchronization signal estimated by the conventional and the QPLL system under single-phase to ground fault.

condition. It is observed that for the conventional PLL, the negative sequence of the grid voltage causes a double-frequency ripple with the error amplitude of 0.45 rad in the extracted phase angle [28]. This erroneous estimation undermines the performance of the DFIG vector control scheme as it produce nonsinusoidal current command signals for the converters. However, the proposed QPLL is completely unaffected to the distortion in the grid voltage waveform.

VI. Conclusion

This paper proposes a novel grid-flux-oriented vector control approach for the RSC and GSC of DFIG-based wind turbines. The QPLL system is used to extract the synchronization signal and equidistant-band VBHCRs are implemented to control the output current of converters. The proposed current regulator is comprised of two multilevel hysteresis comparators integrated with a switching table. The main advantages of this current regulator are the very fast transient response, simple control structure, and intrinsic robustness to the machine parameters variations. It also exhibits an improved steady-state performance as compared to the conventional hysteresis method.

Simulation studies confirm the validity of the proposed grid-flux-oriented vector control scheme under varying wind speed conditions. It is also observed that the ASF of the proposed VBHCR is smaller than the PI current regulator, with an acceptable harmonic distortion in the output current. Finally, the transient responses of the proposed VBHCR and the conventional PI current regulator have been compared under asymmetrical grid fault conditions. Simulations results show that the proposed current regulator has a superior tracking performance that is essentially independent of the grid voltage waveform.

Appendix

The parameters of the simulated DFIG and wind turbine are presented in Tables IV and V, respectively.

TABLE IV
PARAMETERS OF THE SIMULATED DFIG

Rated Power	1.75 MVA
Stator Voltage/Frequency	575 V/ 50 Hz
R_s / R_r	0.00706 pu / 0.005 pu
L_m / L_σ	3.2 pu / 0.32 pu
V_{dc}	1200 Volt

TABLE V
PARAMETERS OF THE SIMULATED WIND TURBINE

Nominal mechanical output power	1.5 MW
Base wind speed	11 m/sec
Maximum power at base wind speed	1.1 MW
Base rotation speed	1.2 pu
Pitch angle	0°

References

[1] T. Ackermann, *Wind Power in Power Systems*. Hoboken, NJ: Wiley, 2005.

[2] R. Pena, J. C. Clare, and G. M. Asher, "Doubly fed induction generator using back-to-back PWM converters and its application to variable-speed wind-energy generation," *IEEE Proc. Electr. Power Appl.*, vol. 143, no. 3, pp. 231–241, May 1996.

[3] G. B. Hopfensper, D. J. Atkinson, and R. A. Lakin, "Stator-flux oriented control of a doubly-fed induction machine with and without position encoder," *IEE Proc. Electr. Power Appl.*, vol. 147, no. 4, pp. 241–250, Jul. 2000.

[4] A. Tapia, G. Tapia, J. X. Ostolaza, and J. R. Saenz, "Modelling and control of a wind turbine driven doubly fed induction generator," *IEEE Trans. Energy Convers.*, vol. 18, no. 2, pp. 194–204, Jun. 2003.

[5] W. Leonhard, *Control of Electrical Drives*. London, U.K.: Springer-Verlag, 2001.

[6] A. Peterson, L. Harnefors, and T. Thiringer, "Comparison between stator-flux and grid flux oriented rotor current control of doubly-fed induction generators," in *Proc. 35th IEEE Power Electr. Spec. Conf.*, 2004, pp. 482–486.

[7] S. Chondrogiannis and M. Barnes, "Stability of doubly-fed induction generator under stator voltage orientated vector control," *IET Gen. Transm. Distrib.*, vol. 2, no. 3, pp. 170–180, 2008.

[8] A. Petersson, L. Harnefors, and T. Thiringer, "Evaluation of current control methods for wind turbines using doubly-Fed induction machines," *IEEE Trans. Power Electron.*, vol. 20, no. 1, pp. 2270–235, Jan. 2005.

[9] J. P. A. Vieira1, M. V. A. Nunes, U. H. Bezerra, and A. C. Nascimento, "Designing optimal controllers for doubly fed induction generators using a genetic algorithm," *IET Gen. Transm. Distrib.*, vol. 3, no. 5, pp. 472–484, 2009.

[10] M. Tsili and S. Papathanassiou, "A review of grid code technical requirements for wind farms," *IET Renew. Power Gen.*, vol. 3, no. 3, pp. 308–332, 2009.

[11] R. Datta and V. T. Ranganathan, "Direct power control of grid-connected wound rotor induction machine without rotor position sensors," *IEEE Trans. Power Electron.*, vol. 16, no. 3, pp. 390–399, May 2001.

[12] K. P. Gokhale, D. W. Karraker, and S. J. Heikkila, "Controller for a wound rotor slip ring induction machine," U.S. Patent 6448735B1, Sep. 2002.

[13] L. Xu and P. Cartwright, "Direct active and reactive power control of DFIG for wind energy generation," *IEEE Trans. Energy Convers.*, vol. 21, no. 3, pp. 750–758, Sep. 2006.

[14] J. Kang and S. Sul, "New direct torque control of induction motor for minimum torque ripple and constant switching frequency," *IEEE Trans. Ind. Appl.*, vol. 35, no. 5, pp. 1076–1082, Sep./Oct. 1999.

[15] Y. S. Lai and J. H. Chen, "A new approach to direct torque control of induction motor drives for constant inverter switching frequency and torque

ripple reduction," *IEEE Trans. Energy Convers.*, vol. 16, no. 3, pp. 220–227, Sep. 2001.

[16] N. R. N. Idris and A. H. M. Yatim, "Direct torque control of induction machines with constant switching frequency and reduced torque ripple," *IEEE Trans. Ind. Electron.*, vol. 51, no. 4, pp. 758–767, Aug. 2004.

[17] D. Zhi and L. Xu, "Direct power control of DFIG with constant switching frequency and improved transient performance," *IEEE Trans. Energy Convers.*, vol. 22, no. 1, pp. 110–118, Mar. 2007.

[18] G. Abad, M. A. Rodriguez, and P. Poza, "Two-level VSC-based predictive direct power control of the doubly fed induction machine with reduced power ripple at low constant switching frequency," *IEEE Trans. Energy Convers.*, vol. 23, no. 2, pp. 570–580, Jun. 2008.

[19] L. Xu, D. Zhi, and A. Williams, "Predictive current control of doubly fed induction generators," *IEEE Trans. Ind. Electr.*, vol. 56, no. 10, pp. 4143–4153, Oct. 2009.

[20] M. Mohseni and S. Islam, "A new vector-based hysteresis current control scheme for three-phase PWM voltage-source inverters," *IEEE Trans. Power Electron.*, to be published.

[21] M. P. Kazmierkowski, M. A. Dzieniakowski, and W. Sulkowski, "Novel space vector based current controllers for PWM-inverters," *IEEE Trans. Power Electron.*, vol. 6, no. 1, pp. 158–166, Jan. 1991.

[22] C. T. Pan and T. Y. Chang, "An improved hysteresis current controller for reducing switching frequency," *IEEE Trans. Power Electron.*, vol. 9, no. 1, pp. 97–104, Jan. 1994.

[23] A. Tilli and A. Tonielli, "Sequential design of hysteresis current controller for three-phase inverter," *IEEE Trans. Ind. Electron.*, vol. 45, no. 5, pp. 771–781, Oct. 1998.

[24] B. H. Kwon, T. W. Kim, and J. H. Youn, "A novel SVM-based hysteresis current controller," *IEEE Trans. Power Electron.*, vol. 13, no. 2, pp. 297–307, Mar. 1998.

[25] B. H. Kwon, B. D. Min, and J. H. Youm, "An improved space-vector-based hysteresis current controller," *IEEE Trans. Ind. Electron.*, vol. 45, no. 5, pp. 752–760, Oct. 1998.

[26] G. R. Slemon, "Modelling of induction machines for electric drives," *IEEE Trans. Ind. Appl.*, vol. 25, no. 6, pp. 1121–1131, Nov./Dec. 1989.

[27] F. K. A. Lima, A. Luna, P. Rodriguez, E. H. Watanabe, and F. Blaabjerg, "Rotor voltage dynamics in the doubly fed induction generator during grid faults," *IEEE Trans. Power Electron.*, vol. 25, no. 1, pp. 118–130, Jan. 2010.

[28] V. Timbus, M. Ciobotaru, R. Teodorescu, and F. Blaabjerg, "Adaptive resonant controller for grid-connected converters in distributed power genaration systems," in *Proc. IEEE APEC 2006*, pp. 1601–1606.

[29] M. Karimi-Ghartemani, H. Karimi, and M. R. Iravani, "A magnitude/phase-locked loop system based on estimation of frequency and inphase/quadrature-phase amplitudes," *IEEE Trans. Ind. Electron.*, vol. 51, no. 2, pp. 511–517, Apr. 2004.

[30] Siegfried Heier, *Grid Integration of Wind Energy Conversion Systems*, 2nd ed. New York: Wiley, 2006.

[31] L. Malesani and P. Tenti, "A novel hysteresis control method for current controlled VSI PWM inverters with constant modulation frequency," *IEEE Trans. Ind. Appl.*, vol. 26, no. 1, pp. 88–92, Jan./Feb. 1990.

[32] L. Malesani, P. Mattavelli, and P. Tomasin, "Improved constant-frequency hysteresis current control for VSI inverters with simple feedforward bandwidth prediction," *IEEE Trans. Ind. Appl.*, vol. 33, no. 5, pp. 1194–1202, Sep./Oct. 1997.

[33] P. N. Tekwani, R. S. Kanchan, and K. Gopakumar, "Novel current error space phasor based hysteresis controller using parabolic bands for control of switching frequency variations," *IEEE Trans. Ind. Electron.*, vol. 54, no. 5, pp. 2648–2656, Oct. 2007.

[34] K. M. Rahman, M. R. Khan, M. A. Choudhury, and M. A. Rahman, "Variable band hysteresis current controllers for PWM voltage source inverters," *IEEE Trans. Power Electron.*, vol. 12, no. 6, pp. 964–970, Nov. 1997.

[35] A. Timbus, M. Liserre, R. Teodorescu, P. Rodriguez, and F. Blaabjerg, "Evaluation of current controllers for distributed power generation systems," *IEEE Trans. Power Electron.*, vol. 24, no. 3, pp. 654–664, Mar. 2009.

[36] L. Harnefors and H.-P. Nee, "Model-based current control of ac machines using the internal model control method," *IEEE Trans. Ind. Appl.*, vol. 34, no. 1, pp. 133–141, Jan./Feb. 1998.

[37] *IEEE Standard for Interconnecting Distributed Resources with Electric Power Systems*, IEEE Standard 15471, 2003.

[38] *Wind Turbines, Measurement and Assessment of Power Quality Characteristics of Grid Connected Wind Turbines—Part 21*, IEC Standard 61400–21, 2008.

[39] M. H. J. Bollen, *Understanding Power Quality Problems—Voltage Sags and Interruptions*. New York: IEEE Press, 2000.

[40] J. Lopez, E. Gubia, P. Sanchis, X. Roboam, and L. Marroyo, "Wind turbines based on doubly fed induction generator under asymmetrical voltage dips," *IEEE Trans. Energy Convers.*, vol. 23, no. 1, pp. 321–330, Mar. 2008.

[41] L. Xu, "Coordinated control of DFIG's rotor and grid side converters during network unbalance," *IEEE Trans. Power Electron.*, vol. 23, no. 3, pp. 1041–1049, May 2008.

[42] J. Hu, Y. He, L. Xu, and B. Williams, "Improved control of DFIG systems during network unbalance using PI-R current regulators," *IEEE Trans. Ind. Electron.*, vol. 56, no. 2, pp. 439–451, Feb. 2009.

Mansour Mohseni (S'09) received the B.Sc. and M.Sc. degrees in electrical engineering from Shahid Chamran University, Ahwaz, Iran, in 2004 and 2007, respectively. He is currently working toward the Ph.D. degree from Curtin University of Technology, Perth, Australia.

His current research interests include wind power generation, grid integration of renewable energy systems, and power electronics.

Syed M. Islam (S'81–M'83–SM'93) received the B.Sc. and M.Sc. degrees in 1979 and 1983, respectively, and the Ph.D. degree from KFUPM in 1988, all in electrical power engineering.

He is currently the Chair Professor in electrical power engineering and the Head of Department of Electrical and Computer Engineering, Curtin University of Technology, Perth, Australia. He has authored or coauthored more than 170 technical papers in his area of expertise. His research interests include the condition monitoring of transformers, wind energy conversion, power quality and harmonics, and power systems.

Dr. Islam was the recipient of the IEEE T Burke Haye's Faculty Recognition Award in 2000. He has been a Keynote Speaker and an Invited Speaker at many international workshops and conferences. He is currently the Vice-Chair of the Australasian Committee for Power Engineering and a member of the Board of Directors of the Australian Power Academy. He is a Fellow of the Engineers Australia, a Senior Member of the IEEE Industry Application Society, Power and Energy Society, and Dielectrics and Electrical Insulation Society, a Fellow of the Institute of Engineering and Technology (IET), and a Chartered Engineer in U.K. He is a Regular Reviewer for the IEEE TRANSACTION ON ENERGY CONVERSION AND POWER DELIVERY. He is an Editor of the IEEE TRANSACTION ON SUSTAINABLE ENERGY.

Mohammad A. S. Masoum (S'88–M'91–SM'05) received the B.S., M.S. and Ph.D. degrees in electrical and computer engineering from the University of Colorado at Boulder, in 1983, 1985, and 1991, respectively.

He is currently an Associate Professor and the Head of discipline for electrical power engineering at the Electrical and Computer Engineering Department, Curtin University of Technology, Perth, Australia. He is the Co-Author of *Power Quality in Power Systems and Electrical Machines* (San Diego, CA: Academic Press, Elsevier, 2008). His research interests include optimization, power quality, and stability of power systems and distributed generation.